Comparison of ATMS Striping Noise Between NOAA-20 and S-NPP and Noise Impact on Warm Core Retrieval of Typhoon Jelawat (2018)

Xiaolei Zou, *Member, IEEE*, and Xiaoxu Tian

***Abstract*—The Advanced Technology Microwave Sounder (ATMS) is onboard both the National Oceanic and Atmospheric Administration (NOAA)-20 and the Suomi National Polar-Orbiting Partnership (S-NPP) satellites. NOAA-20 has the same sun-synchronous orbit as that of the S-NPP, but is 50 min (i.e., half orbit) ahead. The striping noise is found in ATMS brightness temperature observations from both NOAA-20 and S-NPP. In this study, first, a striping noise detection and mitigation algorithm that was previously developed for striping noise mitigation in ATMS observations from S-NPP is adopted to characterize the striping noise in NOAA-20 ATMS brightness temperature measurements. It combines a principal component analysis and an ensemble empirical mode decomposition method. It is found that the magnitudes of both the striping noise and the random noise in NOAA-20 ATMS data are smaller than those in S-NPP ATMS data. Second, global positioning system radio occultation retrieved temperature profiles are used as the training dataset for ATMS hurricane warm core retrievals in order to investigate the impacts of the data noise. Numerical results are demonstrated using the case of Typhoon Jelawat (2018), which rapidly intensified from a Category 1 to a Category 4 super typhoon and weakened back to Category 1 within 24 h. Finally, we show that a half-orbit separation of NOAA-20 from S-NPP enables the rapidly evolving vertical structures of Typhoon Jelawat. This suggests an enhanced tropical cyclone monitoring capability offered by NOAA-20 and S-NPP for this hurricane season and a few following years.**

***Index Terms*—Advanced Technology Microwave Sounder (ATMS), National Oceanic and Atmospheric Administration (NOAA)-20, striping noise, tropical cyclone (TC), typhoon, warm core.**

I. Introduction

THE National Oceanic and Atmospheric Administration (NOAA)-20 satellite, previously known as the Joint Polar Satellite System, was successfully launched on November 18, 2017 into the same sun-synchronous orbit (altitude of ∼830 km) as that of the Suomi National Polar-Orbiting Partnership (S-NPP) satellite. NOAA-20 flies a half-orbit (∼50 min) ahead of S-NPP and scans the earth 14 times daily. This arrangement enables a significant amount of overlap in observational coverage. The Advanced Technology Microwave Sounder (ATMS) is carried by both NOAA-20 and S-NPP. The ATMS is a microwave cross-track radiometer with 22 channels. Its radiance observations at temperature-sounding channels (channels 5–15) provide atmospheric temperature profile information from the earth's surface up to the stratosphere [1]–[3]. Radiance observations made by the ATMS onboard S-NPP had positive impacts on numerical weather predictions [4], [5]. NOAA-20 orbiting along with S-NPP enables an improved temporal coverage with ATMS observations over the globe four times daily. Should S-NPP cease to operate in the future, NOAA-20 will ensure the continuity of observational data from the ATMS and other instruments carried by both satellites.

From the on-orbit measurements of the S-NPP ATMS in 2011, flicker noise in the along-track direction, manifested as striping-patterned noise, was spotted in the difference fields between the observed and numerical weather prediction model background simulated brightness temperatures (O-B) [4], [6]. In contrast, no striping noise was found in measurements of the Advanced Microwave Sounding Unit (AMSU)-A, the predecessor of ATMS. Qin *et al.* [6] proposed a striping noise detection algorithm for S-NPP ATMS observations. The brightness temperatures over a segment of a swath are first decomposed with the principal component analysis (PCA) into different principal component (PC) modes (i.e., eigenvectors). The striping noise was believed to be located in the first PC mode. An ensemble empirical mode decomposition (EEMD) method is then applied to the first PC mode to remove high-frequency random noise [7], [8]. It was demonstrated that this method with PCA and EEMD combined could remove the striping noise without affecting weather signals in the observations. Nonetheless, the method described in [6] is not applicable to ATMS window channels whose radiance measurements have sharp gradients in the presence of thick clouds and land/ocean interfaces. Zou *et al.* [9] discussed this deficiency in the detection method and proposed an improved PCA/EEMD striping noise mitigation method that is applicable to all 22 ATMS channels.

Tropical cyclones (TCs) generally emerge and develop over oceans, where conventional *in situ* observations are rare over oceans. Airborne data may be available for some storm events

Manuscript received September 14, 2018; revised December 12, 2018; accepted January 5, 2019. This work was supported by the National Oceanic and Atmospheric Administration (NOAA) under Grant NA14NES4320003. *(Corresponding author: Xiaolei Zou.)*

The authors are with the Earth System Science Interdisciplinary Center, University of Maryland, College Park, MD 20740 USA (e-mail: xzou1@umd.edu; xtian15@terpmail.umd.edu).

Digital Object Identifier 10.1109/JSTARS.2019.2891683

but are still very limited in spatial coverage not available when TCs are in deep oceans. In comparison, satellite observations are much more abundant over oceans. Geostationary satellites can provide radiance observations at visible or infrared wavelengths with high spatial and high temporal resolutions. Such satellites include the Geostationary Operational Environmental Satellite series observing the East Pacific Ocean and the West Atlantic Ocean, and Himawari-8/-9 satellites and FengYun-2/-4 satellites covering the West Pacific Ocean and the Indian Ocean [10], [11]. Polar-orbiting satellites such as NOAA-20 and S-NPP carry several common instruments that make measurements in the visible, infrared, and microwave spectral regions and cover the majority of the earth twice a day. A primary limitation of the instruments observing at visible or infrared wavelengths is that they cannot penetrate clouds. Weather phenomena such as TCs involve clouds of large extents. In the presence of clouds, structures beneath the cloud top cannot be observed at visible or infrared wavelengths. Microwave instruments like the ATMS, however, can observe radiances of the atmospheric profile in almost all weather conditions except for heavy precipitation. Microwave temperature sounder data have been used to estimate TC size and intensity and to improve hurricane forecasts [1], [2], [12]–[15]. Typhoon Jelawat (2018) was the first Category 4 super-typhoon of 2018 that was developed over the West Pacific Ocean and reached a maximum 1-min sustained wind of 130 kn (67 $\mathrm{m \cdot s^{-1}}$) [16]. It experienced a rapid intensification from a Category 1 typhoon at 0000 UTC March 29, 2018 to Category 4 at ∼1500 UTC the same day. The storm quickly weakened to Category 2 on March 30, 2018 and a tropical storm on March 31, 2018.

In this study, the PCA/EEMD striping noise mitigation method described in [9] is applied to NOAA-20 ATMS measurements to characterize the striping noise. The orbit arrangements of NOAA-20 and S-NPP as well as some ATMS instrument features will be introduced in Section II. A brief description of the methodology and comparisons of the detected striping noise in NOAA-20 and S-NPP ATMS will be given in Section III. A global positioning system (GPS) radio occultation (RO) trained temperature profile retrieval algorithm is then applied to destriped ATMS observations from both satellites, and the three-dimensional (3-D) structural evolution of Typhoon Jelawat is analyzed in Section IV.

II. Satellite Orbit and ATMS Instrument Features

The S-NPP ascending swath crosses the equator at 0130 local time. NOAA-20 is a half orbit or 50 min ahead of S-NPP. Fig. 1(a) illustrates the footprints of two neighboring ascending swaths of NOAA-20 and S-NPP, as well as their overlapping area on March 29, 2018. Fig. 1(b) and (c) shows the time segments of the swaths. At 0400 UTC, NOAA-20 is above the North Pole, while S-NPP is above the South Pole a half-orbit away. The background black-and-white image shows the 10.4-μm TBs observed by the Advanced Himawari Imager (AHI) onboard the Himawari-8 geostationary satellite [10]. To the east of the Philippines is Typhoon Jelawat. When S-NPP and NOAA-20 were orbiting one after the other, the typhoon center was observed in the ATMS swaths of both satellites only 50 min apart.

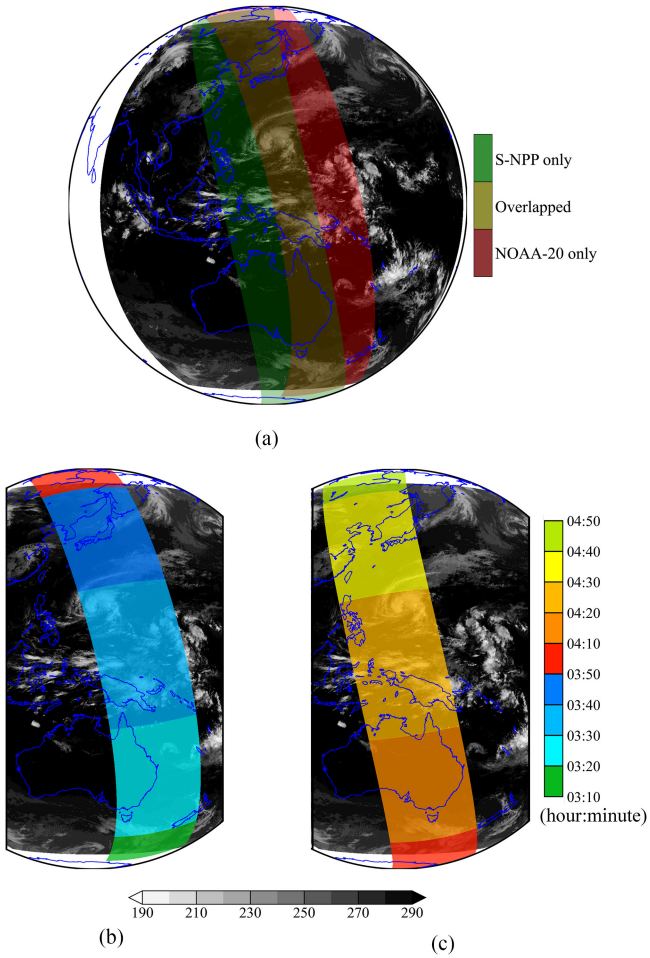

Fig. 1. Two neighboring NOAA-20 and S-NPP swaths showing (a) the overlapping portion (brown) and nonoverlapping portions (red for NOAA-20 only and green for S-NPP only) on March 29, 2018. Observation times of the two swaths in (a) for (b) NOAA-20 and (c) S-NPP (multicolored colorbar). The background images in (b) and (c) show AHI channel 13 (10.45 μm) brightness temperatures (unit: K) at 0400 UTC March 29, 2018 (grayscale colorbar).

The ATMS onboard NOAA-20 has the same 22 channels as the ATMS onboard S-NPP with the first 16 channels for temperature-sounding purposes and the rest for humidity soundings. Channels 1–2, 3–16, and 17–22 have beam widths of 5.5°, 2.2°, and 1.1°, respectively. Tian *et al.* [17] proposed to characterize the noise equivalent differential temperature (NEDT) for the ATMS onboard S-NPP using the Allen deviation method, which produces a stable and consistent noise characterization of the instrument. Fig. 2 shows the NEDTs in terms of the Allen deviation for all 22 channels of the ATMS onboard NOAA-20 and S-NPP. The instrument noise of the ATMS on NOAA-20 is lower than that of the ATMS onboard S-NPP. The interim reanalysis dataset from the European Centre for Medium-Range Weather Forecasts (ECMWF), representing background information, was used as input to the Community Radiative Transfer

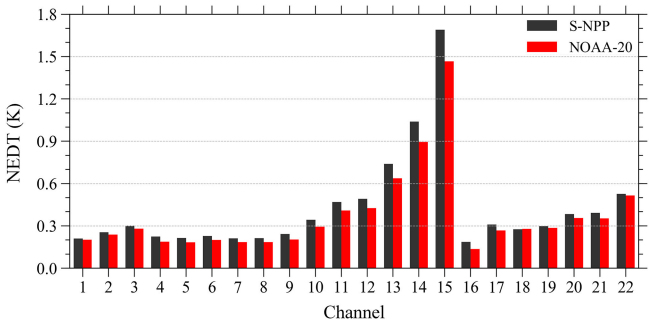

Fig. 2. Noise equivalent differential temperatures (NEDTs) for ATMS channels 1–22 from S-NPP (black bars) and NOAA-20 (red bars).

Model (CRTM) to simulate the antenna temperatures of the ATMS onboard both S-NPP and NOAA-20.

III. Brief Description of the Striping Noise Mitigation Algorithm

A data matrix consists of brightness temperature observations from a segment of a swath with 300 scan lines and can be written as

$$\mathbf{A} = \begin{pmatrix} T_b^{\text{obs}}(1,1) & \cdots & T_b^{\text{obs}}(1,N) \\ \vdots & \ddots & \vdots \\ T_b^{\text{obs}}(M,1) & \cdots & T_b^{\text{obs}}(M,N) \end{pmatrix}. \quad (1)$$

The eigenvalues and eigenvectors can be obtained by solving the following equation:

$$\mathbf{A}\mathbf{A}^T\mathbf{e}_i = \lambda_i \mathbf{e}_i. \quad (2)$$

The vector $\mathbf{e}_i$ is the *i*th eigenvector of the covariance matrix $\mathbf{A}\mathbf{A}^T$. The resulted eigenvalues have descending values, i.e., $\lambda_1 > \lambda_2 > \cdots > \lambda_{96}$. Therefore, the first corresponding eigenvector accounts for the greatest variance in the data matrix $\mathbf{A}$, second accounting for the second greatest, and so on. A set of PC coefficients ($\mathbf{U}$) can then be calculated as

$$\mathbf{U} = \mathbf{E}^T\mathbf{A} = \begin{pmatrix} \mathbf{u}_1^T \\ \mathbf{u}_2^T \\ \vdots \\ \mathbf{u}_{96}^T \end{pmatrix} \equiv \begin{pmatrix} \mathbf{e}_1 & \mathbf{e}_2 & \cdots & \mathbf{e}_{96} \end{pmatrix}^T \mathbf{A}. \quad (3)$$

Therefore, the *i*th PC mode can be defined as

$$\mathbf{P}_i = \sum_{k=1}^{96}\sum_{j=1}^{N} e_i(k)\, u_i(j) \,(i = 1, 2, \ldots, 96). \quad (4)$$

The original brightness temperature data matrix can be exactly reconstructed as

$$\mathbf{A} = \sum_{i=1}^{96} \mathbf{P}_i. \quad (5)$$

The striping noise seen in the ATMS observations is high-frequency random fluctuations in the first three PC modes ($\mathbf{P}_1$, $\mathbf{P}_2$, and $\mathbf{P}_3$). An ensemble empirical model decomposition method can then be applied to the first PC coefficients ($\mathbf{u}_1$, $\mathbf{u}_2$, and $\mathbf{u}_3$) and isolate the high-frequency noise from the PC modes [8]. The intrinsic mode function (IMF) with the highest to lowest frequencies can be sequentially extracted in the PC coefficients, representing signals with the highest to lowest frequencies. To extract each IMF, the local maxima and minima in $\mathbf{u}_i (i = 1, 2, \text{ and } 3)$ are first identified and connected through a cubic spline interpolation to form an upper envelope with all the maxima and a lower envelope with all the minima. The first IMF $(C_{i,1})$ of $\mathbf{u}_i$ can be obtained as the differences between $\mathbf{u}_i$ and the average of the upper and lower envelope $(a_{i,1})$ as

$$C_{i,1}(j) = R_{i,0}(j) - a_{1,1}(j) \quad (6)$$

where $R_{i,0}(j)(j = 1, 2, \ldots, N)$ denotes $\mathbf{u}_i$. The PC coefficients $\mathbf{u}_i$ with the highest frequency signals isolated can be written as

$$R_{i,1}(j) = u_i(j) - C_{i,1}(j). \quad (7)$$

The second and third IMFs $(C_{i,2}$ and $C_{i,3})$ can be sequentially extracted from $R_{i,1}$ to obtain $R_{i,2}$ and $R_{i,3}$. The resulting PC coefficients can be expressed as

$$u_i(j) = u_i j - \sum_{m=1}^{M_i} C_{i,m}(j) \quad (8)$$

where M_1 represents the total number of IMFs to be removed from each of the first three PC coefficients. The specific values of M_1 for each of the 22 channels are detailed in the last column of Table I. The data matrix with striping noise mitigated can be reconstructed as

$$\mathbf{A}^{\text{destriped}} = \sum_{i=1}^{3} \mathbf{P}_i^{\text{destriped}} + \sum_{i=4}^{96} \mathbf{P}_i. \quad (9)$$

The striping patterned noise is more discernible in the differences between the brightness temperature observations and CRTM simulations (O-B) [6]. In this study, the ECMWF interim dataset is taken to serve as the background information for CRTM input for ATMS brightness temperature simulations. In Fig. 3, the O-B before (left panels) and after (middle panels) destriping is for both S-NPP and NOAA-20 ATMS measurements is shown. The detected striping noise patterns are given in the right panels. Comparing the raw observations (left panels) between NOAA-20 and S-NPP ATMS, the striping patterns can be seen in both panels, with those in the results for S-NPP ATMS slightly more obvious. In the results after destriping (middle panels), the striping patterned noise is removed in both cases. The detected striping noise for S-NPP ATMS has larger magnitudes than that from NOAA-20 ATMS. This is true globally (see Fig. 4). Fig. 5 shows the power spectrum density (PSD) of O-B at channel 9 in a frequency domain. Before destriping at about 10^{-1} s^{-1}, the PSD for S-NPP ATMS (solid red curve) is greater than that of NOAA-20 ATMS (solid blue curve), agreeing with the results in Fig. 3. After destriping (opaque blue and red curves), the noise level of both ATMS instruments came down to the same level, indicating efficient noise mitigation. Expanding the striping noise detection results over global range,

TABLE I
CHANNEL-DEPENDENT CENTER FREQUENCIES, THRESHOLDS USED IN THE FIRST STEP OF THE MODIFIED DESTRIPING ALGORITHM, AND THE TOTAL NUMBER OF IMFS REMOVED FROM EACH OF THE FIRST THREE PC MODES FOR ATMS CHANNELS 1–22

Channel Number	Frequency (GHz)	Threshold (K)	PCA1/PCA2/PCA3 Numbers of IMFs removed
1	23.8	1.0	1/1/1
2	31.4	1.2	
3	50.3	1.3	
4	51.76	1.3	
5	52.8	0.8	
6	53.596±0.115	-	
7	54.4	-	3/2/2
8	54.94	-	3/3/3
9	55.5	-	
10	57.2903	-	
11	57.2903±0.217	-	
12	57.2903±0.322±0.048	-	
13	57.2903±0.322±0.022	-	
14	57.2903±0.322±0.010	-	
15	57.2903±0.322±0.004	-	
16	88.20	2.0	1/1/1
17	165.5	1.6	
18	183.31±7	1.4	
19	183.31±4.5	5.0	
20	183.31±3	2.5	
21	183.31±1.8	3.0	
22	183.31±1.0	-	

the striping noise in NOAA-20 ATMS is less severe than that in S-NPP ATMS globally.

IV. ATMS WARM CORE RETRIEVALS

Tian and Zou [1] proposed a refined temperature retrieval algorithm, including only a subset channels when retrieving temperatures at a given pressure level, and that removes the scan-dependent biases in the retrieved atmospheric temperatures. The retrieval algorithm was then applied to measurements from all functional AMSU-A instrument onboard NOAA satellites to analyze the temporal evolutions of thermal structures in Hurricanes Harvey, Irma, and Maria (2017) [3]. The regression coefficients have to be trained using the TB at each field-of-view (FOV) position. Temperature profiles from GPS ROs were used as the training dataset to obtain better accuracies [2]. However, the geographical distribution of RO profiles is random around the globe, and the sample number of RO profiles collocated with NOAA-20 ATMS observations is small. To address this difficulty, in this study, the limb correction method described by in Goldberg *et al.* [18], Zhang *et al.* [19], and Tian *et al.* [20] was first applied to ATMS observations to remove scan-dependent variations. Limb-corrected TBs will contain only weather information regardless of their FOV positions. The regression coefficients can then be trained with ATMS TBs and temperature profiles from GPS ROs as follows:

$$T^{\mathrm{RO}}(p) = C_0(p) + \sum_{i=i_{1,p}}^{i_{2,p}} C_i(p)\, T_b^{\mathrm{obs}}(i) \tag{10}$$

where p is the pressure and $(i_{1,p}, i_{1,p}+1, i_{1,p}+2, \cdots i_{2,p})$ is a subset of ATMS channels 5–15 correlated with atmospheric temperatures at pressure level p. $T^{\mathrm{RO}}(p)$ are RO-derived temperatures collocated with ATMS observations with collocation criteria of no more than a 100-km distance and a 3-h time difference. C_0 and $C_{\mathrm{i}}(p)$ are the regression coefficients to be trained.

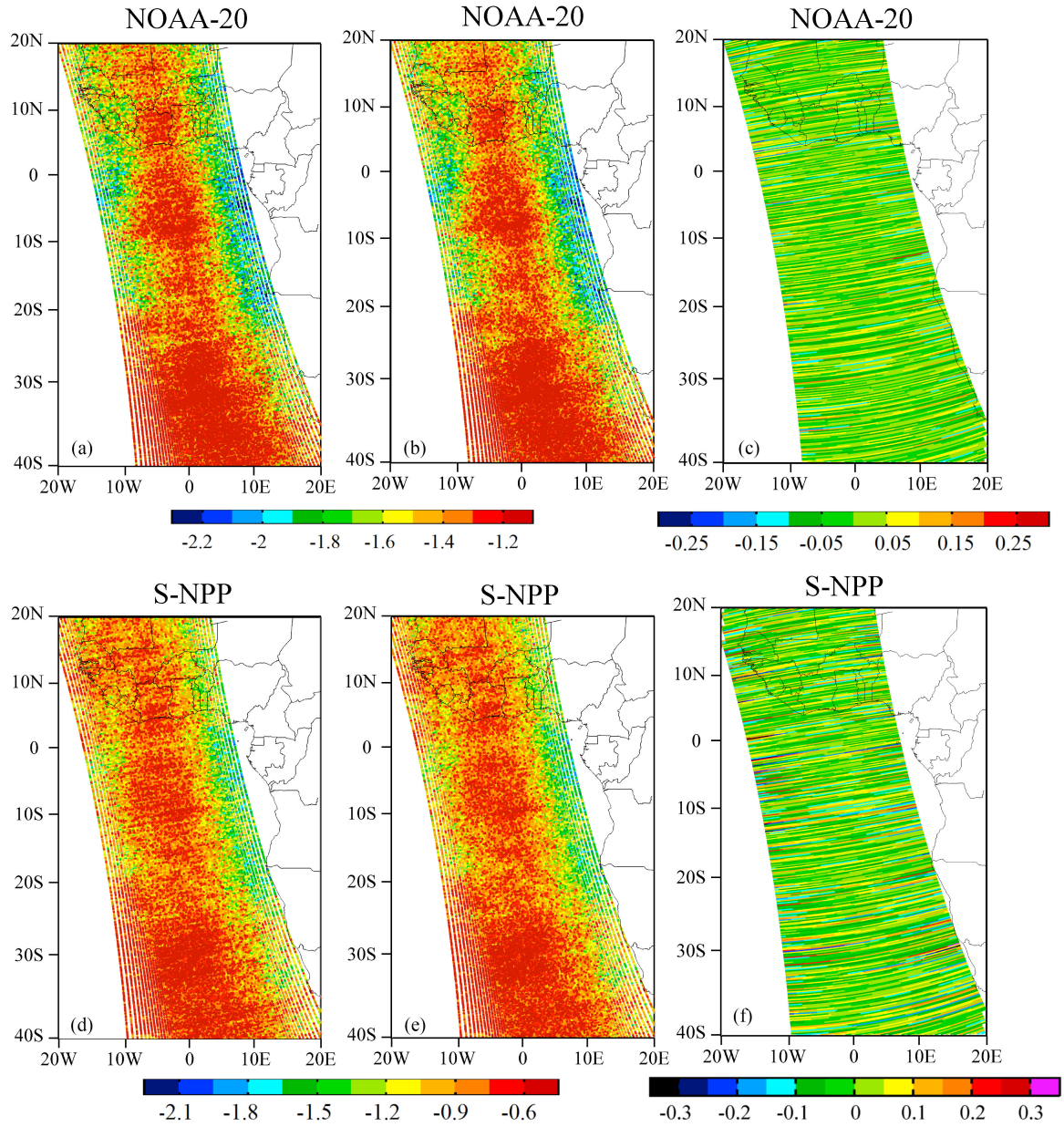

Fig. 3. Spatial distributions of the differences of antenna temperature of ATMS channel 9 between observations and simulations without (left panels) and with a striping noise mitigation (middle panels), as well as the striping noise (right panels) on December 29, 2017 from (a)–(c) NOAA-20 and (d)–(f) S-NPP.

Regression coefficients for S-NPP and NOAA-20 ATMS temperature retrievals are performed separately. Clear-sky and cloudy-sky sets of coefficients are generated for each instrument. For clear-sky conditions, channels 5–15 are included in (10). For cloudy conditions, only channels 8–15 are included because channels 5–7 are prone to rain contamination. The coefficients were trained using ATMS observations from February 20, 2018 to March 23, 2018 and collocated GPS RO profiles.

Typhoon Jelawat (2018) was the first super-typhoon of 2018 observed in the West Pacific Ocean, which reached a maximum sustained wind of 130 kn (67 $\mathrm{m \cdot s^{-1}}$). A temperature warm anomaly field was first calculated to analyze the evolution of the 3-D thermal structure of the storm during this rapidly changing transitional period. The difference between atmospheric temperatures and ambient temperatures, i.e., mean temperatures within 15° × 15° latitude/longitude grid boxes with the storm perturbation excluded, defines the typhoon warm-core anomaly field. The 34-kn wind radius determines the storm size. Fig. 6 shows the temperature anomalies at 250 hPa retrieved with NOAA-20 ATMS observations at 0330 UTC March 29, 2018 before [see Fig. 6(a)] and after [see Fig. 6(b)] destriping. The differences between the two are given in Fig. 6(d). The minimum and maximum values of the striping noise are −0.86 and 0.70 K, respectively. The destriping method effectively removes the impacts of striping noise on the ATMS temperature retrievals. In order to investigate the impact of not only the striping noise but also the random noise on the warm core retrieval, the footprint remapping method described in [2] and [21] is also applied to

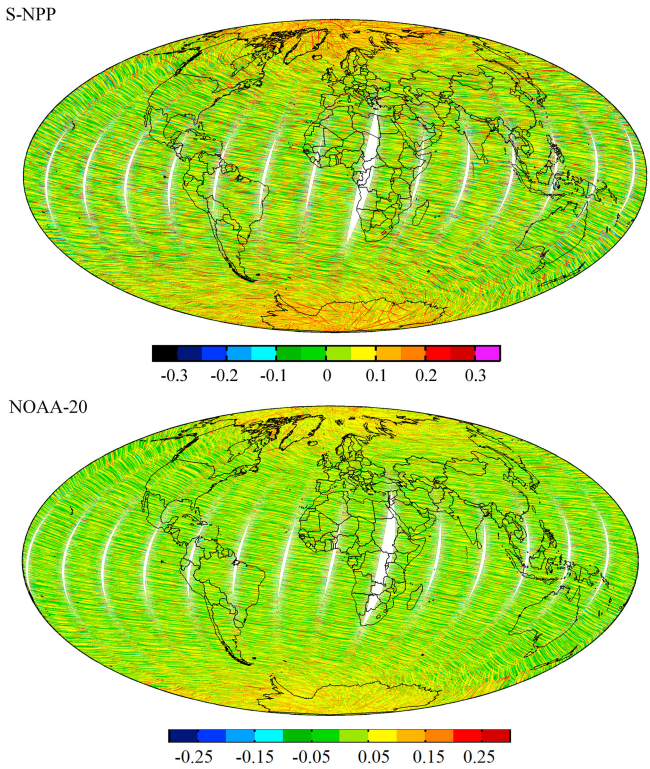

Fig. 4. Global distributions of striping noise extracted from antenna temperature observations of ATMS channel 9 from S-NPP (top panel) and NOAA-20 (bottom panel) on January 15, 2018.

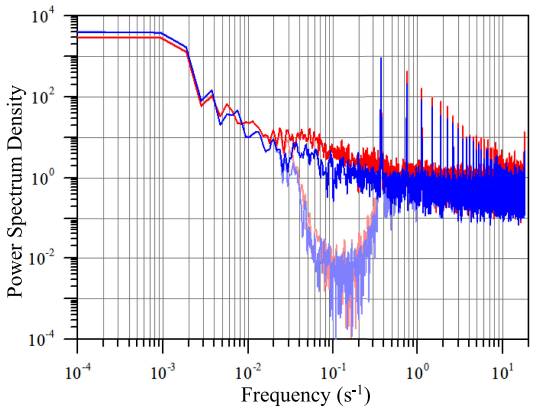

Fig. 5. Power spectrum density distributions of the differences of antenna temperature of ATMS channel 9 between observations and simulations from NOAA-20 (blue) and S-NPP (red) on December 29, 2017 before (top two curves near the frequency 10^{-1} s^{-1}) and after (the two dip-down curves near the frequency 10^{-1} s^{-1}) removing the striping noise.

the destriped brightness temperatures [see Fig. 6(c)]. It is seen that the differences between Fig. 6(a) and (c) can exceed ± 0.1 K [see Fig. 6(e)]. It is seen that the striping noise [see Fig. 6(d)] is only half of the sum of the striping and random noises [see Fig. 6(e)] in the temperature retrieval from NOAA-20 ATMS observations.

Typhoon Jelawat rapidly intensified from Category 1 at 0000 UTC March 29, 2018 to Category 4 at ∼1500 UTC March 29, 2018 [16]. The strong vertical wind shear in the surrounding

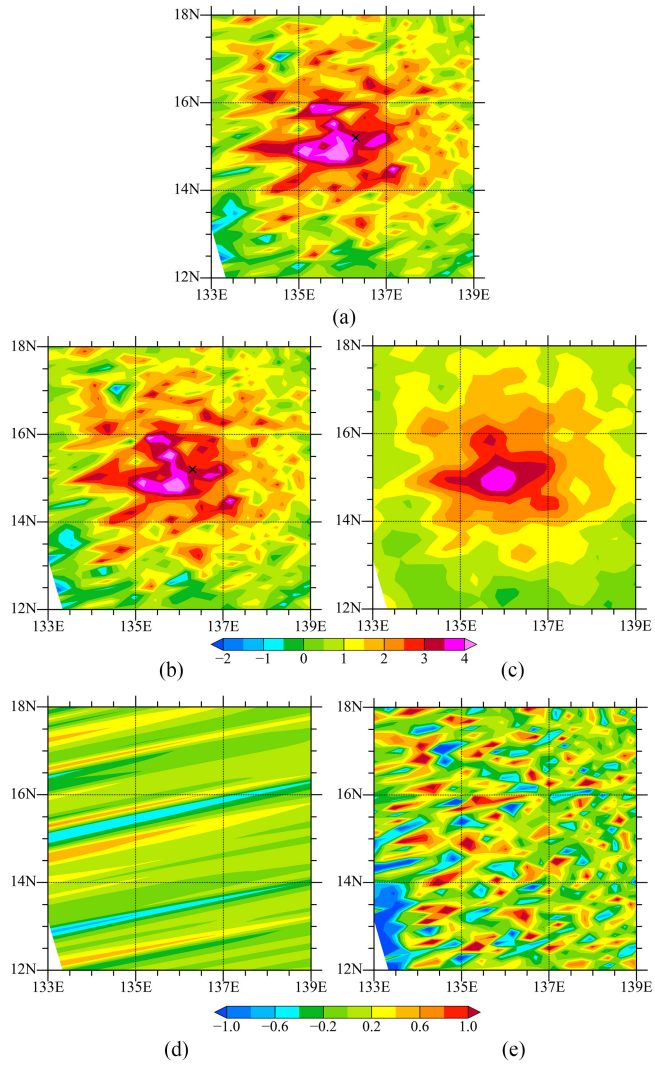

Fig. 6. Temperature anomalies at 250 hPa retrieved with NOAA-20 ATMS observations (a) without any noise suppression, (b) after destriping, and (c) after remap at 0338 UTC March 29, 2018. (d) Difference between (a) and (b). (e) Difference between (a) and (c).

environment stopped the typhoon from intensifying further. The storm then weakened rapidly to Category 1. Vertical wind shear is an important inhibitive factor for TC development [22]–[24]. Fig. 7(a) (NOAA-20) and (b) (S-NPP) shows the vertical warm-core cross sections of Typhoon Jelawat starting from 0000 UTC March 29, 2018. The dashed curve shows the evolution of vertical wind shear obtained by averaging the wind speed differences of wind vectors between 200 and 850 hPa within a radius of 500 km from the typhoon center, which are calculated from the National Center for Environmental Prediction Global Forecast System analysis dataset. At ∼0400 UTC March 29, 2018, the warm cores captured by both NOAA-20 and S-NPP appear well defined. The vertical wind shear values are less than 15 $m \cdot s^{-1}$ at this time. The next overpass by NOAA-20 at ∼1600 UTC March 29, 2018 shows a stronger warm core, which suggests a stronger storm intensity. The S-NPP overpass, which is 50 min later than NOAA-20, shows a tilted vertical warm structure in the presence of increasing vertical wind shear. The warm core redefined on

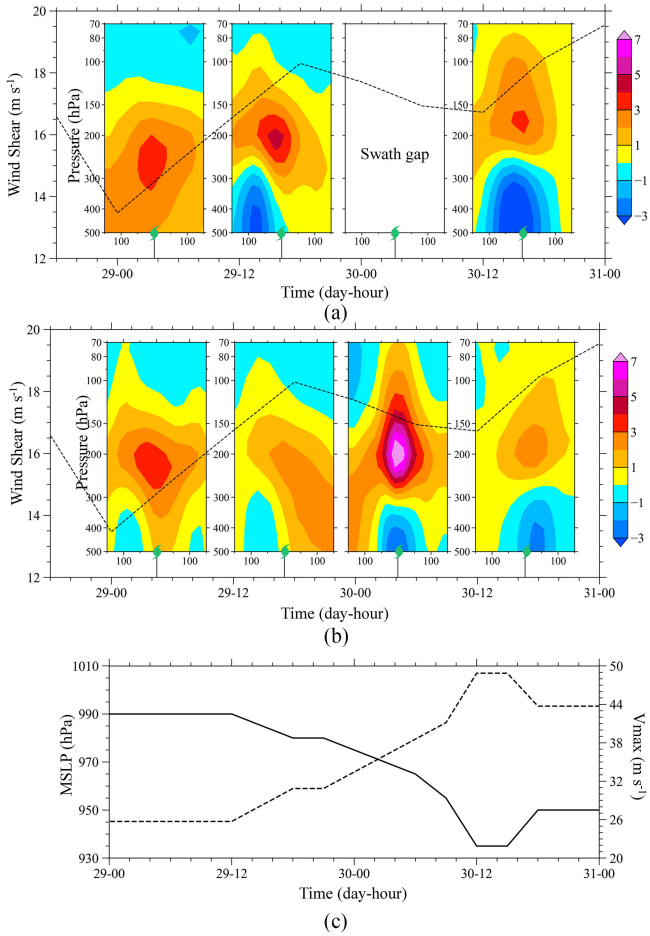

Fig. 7. Time evolution of the vertical cross sections of the temperature anomaly obtained from the ATMS onboard (a) NOAA-20 and (b) S-NPP from 0000 UTC March 29, 2018 to 0000 UTC March 31, 2018 when Typhoon Jelawat intensified from Category 1 at 0000 UTC March 29, 2018 to Category 2 at 1200 UTC March 30, 2018 then weakened slightly afterward. (c) Temporal evolutions of the minimum sea level pressure (MSLP) and the maximum wind speed (*V*max) from Best Track records. The dashed curves in (a) and (b) show the evolution of vertical wind shear obtained by averaging the wind speed differences of wind vectors between 200 and 850 hPa within a radius of 500 km from the typhoon center (green hurricane symbol).

March 30, 2018 as the wind shear slightly decreased. Fig. 7(c) shows the evolution of the minimum sea level pressure and the maximum wind speed from Best Track records. Because the storm reached its peak intensity of 130 kn only briefly, the Best Track was not able to pick up this fast-evolving process.

Fig. 8 shows the horizontal temperature anomaly distributions from 1610 UTC March 29, 2018 to 0410 UTC March 30, 2018. The rapid weakening process during the 50 min from 1610 UTC [see Fig. 8(a)] to 1701 UTC [see Fig. 8(b)] was captured by the back-to-back observational setup of NOAA-20 and S-NPP. The first observation by NOAA-20 on March 30, 2018 was not able to cover the storm center entirely because it fell into a gap between swaths. The eastern side of the warm core, however, was still resolved near the swath edges of the ATMS on NOAA-20 [see Fig. 8(c)]. The temperature anomaly results from ATMS observations on March 30, 2018 show a well-defined warm core structure [see Fig. 8(d)]. Brightness temperatures at 10.4 μm

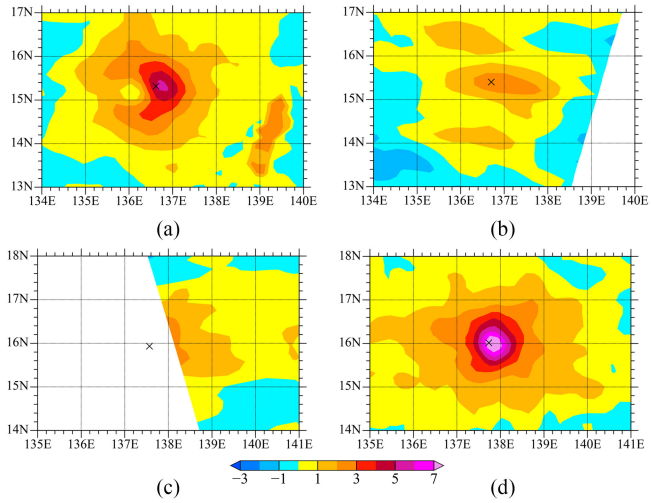

Fig. 8. Temperature anomalies (unit: K) at 200 hPa retrieved from the ATMS onboard NOAA-20 (left panels) and S-NPP (right panels) at (a) 1610 UTC for NOAA-20 and (b) 1701 UTC for S-NPP on March 29, 2018, and (c) 0320 UTC for NOAA-20 and (d) 0410 UTC for S-NPP on March 30, 2018. The black cross shows the location of the storm center.

from the AHI onboard Himawari-8 from 1600 UTC March 29, 2018 to 0400 UTC March 30, 2018 are shown in Fig. 9 and offer a more temporally continuous view of Typhoon Jelawat's evolution. At 1600 UTC, a typhoon eye can be spotted near the storm center location given by the Best Track record. At 1730 UTC, close to the time S-NPP was scanning the typhoon, the eye started to disappear. Meanwhile, the vertical wind shear increased from 17.8 to 18.2 $\mathrm{m \cdot s^{-1}}$. Not until 0300 UTC March 30, 2018, when the wind shear decreased to 17.3 $\mathrm{m \cdot s^{-1}}$, did the typhoon eye start to reappear. Although 0300 UTC was close to the observing time of NOAA-20, the storm center happened to fall into the gap between swaths. Nevertheless, half an orbit after NOAA-20 (0410 UTC), the ATMS onboard S-NPP was able to observe a redefined typhoon eye. This back-to-back satellite observational setup ensures the relatively complete coverage of Typhoon Jelawat.

V. Summary and Conclusion

The NOAA-20 satellite shares nearly the same orbit as the S-NPP satellite, flying 50 min ahead of it. This back-to-back orbit arrangement ensures a considerable amount of overlapping observations when both satellites are operational and continuity of observation coverage in case S-NPP ceases operating. The noise levels of ATMS observations from NOAA-20, quantified by the NEDT, are smaller those of S-NPP S for all 22 channels. The scan patterns in observations from both ATMS instruments are nearly the same with minor asymmetry differences. The observations from ATMS onboard NOAA-20 are then examined for striping pattern noise, a problem known to exist with the S-NPP ATMS. A striping noise detection and mitigation algorithm with combining PCA and EEMD is applied to NOAA-20 ATMS measurements as well as to S-NPP ATMS observations during the same period of time. The results showed that, similar to the NEDTs, the striping noise detected in NOAA-20 is also smaller

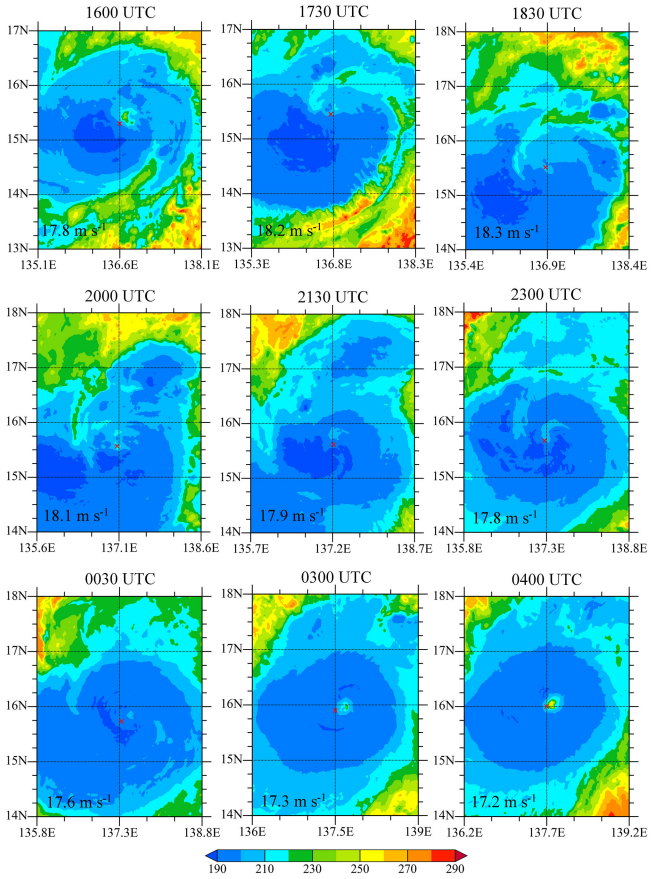

Fig. 9. Nine snapshots showing brightness temperatures at 10.4 μm (unit: K) observed by the AHI onboard Himawari-8 from 1600 UTC March 29, 2018 to 0400 UTC March 30, 2018. Red crosses show the storm centers of Typhoon Jelawat. Wind shear values (calculated as the mean of the differences in wind vectors between the 200- and 850-hPa pressure levels within a 500-km radial distance from the typhoon center) are given at the bottom left of each panel. The red cross shows the location of the storm center.

in magnitudes than those in S-NPP ATMS. This implies an improvement on ATMS instrument design. Using the destriping method, the striping noise in both instruments can be reduced to similar levels.

With a GPS-RO-based temperature retrieval algorithm recently developed in [2], the impacts of striping noise on warm core retrievals are assessed in the case of Typhoon Jelawat, the first super typhoon in 2018. It is shown that the retrieved temperatures can be affected by nearly 1 K if striping noise is not mitigated beforehand. The destriped brightness temperatures are then taken as input into the temperature retrieval algorithm for analyzing the structural evolutions of Typhoon Jelawat. Beginning at 0000 UTC March 29, 2018, Typhoon Jelawat rapidly intensified from a Category 1 typhoon to a Category 4 typhoon. However, the storm quickly weakened to Category 1 the same day due to strong vertical wind shear in its vicinity. These rapid changes were well captured by the NOAA-20- and S-NPP ATMS-retrieved atmospheric temperature fields, thanks to the 50-min difference between NOAA-20 and S-NPP orbital configuration. A set of nine AHI-based snapshots from 1600 UTC March 29, 2018 to 0400 UTC March 30, 2018 further validated this fast-evolving process. The ATMS provides critical information for resolving the 3-D structures of TC events. This improved temporal resolution from two polar-orbiting satellites substantiates the significance of future CubeSat missions that will involve more microwave instruments making more frequent measurements [25].

Acknowledgement

The satellite data employed in this study can be obtained from NOAA's Comprehensive Large Array-data Stewardship System at http://www.class.ncdc.noaa.gov/saa/products/welcome. The temperatures from Global Positioning System Radio Occultation can be found at the European Organisation for the Exploitation of Meteorological Satellites Radio Occultation Meteorology website (http://www.romsaf.org). Results used to generate the figures in this study are available at http://jlrdata.umd.edu/Tianshare/TyphoonJelawat.html

References

[1] X. Tian and X. Zou, "ATMS- and AMSU-A-derived hurricane warm core structures using a modified retrieval algorithm," *J. Geophys. Res.*, vol. 121, pp. 12630–12646, 2016.

[2] X. Zou and X. Tian, "Hurricane warm-core retrievals from AMSU-A and remapped ATMS measurements with rain contamination eliminated," *J. Geophys. Res.*, vol. 123, pp. 10815–10829, 2018.

[3] X. Tian and X. Zou, "Capturing size and intensity changes of hurricanes Irma and Maria (2017) from polar-orbiting satellite microwave radiometers," *J. Atmos. Sci.*, vol. 75, pp. 2509–2522, 2018.

[4] N. Bormann, A. Fouilloux, and W. Bell, "Evaluation and assimilation of ATMS data in the ECMWF system," *J. Geophys. Res.*, vol. 118, pp. 12970–12980, 2013.

[5] X. Zou, F. Weng, B. Zhang, L. Lin, Z. Qin, and V. Tallapragada, "Impacts of assimilation of ATMS data in HWRF on track and intensity forecasts of 2012 four landfall hurricanes," *J. Geophys. Res.*, vol. 118, pp. 11558–11576, 2013.

[6] Z. Qin, X. Zou, and F. Weng, "Analysis of ATMS striping noise from its Earth scene observations," *J. Geophys. Res.*, vol. 118, pp. 13214–13229, 2013.

[7] N. E. Huang and Z. Wu, "A review on Hilbert-Huang transform: Method and its applications to geophysical studies," *Rev. Geophys.*, vol. 46, 2008, Art. no. RG2006.

[8] Z. Wu and N. E. Huang, "Ensemble empirical mode decomposition: A noise-assisted data analysis method," *Adv. Adaptive Data Anal.*, vol. 1, pp. 1–41, 2009.

[9] X. Zou, H. Dong, and Z. Qin, "Striping noise reduction for ATMS window channels using a modified destriping algorithm," *Quart. J. Roy. Meteorol. Soc.*, vol. 143, pp. 2567–2577, 2017.

[10] X. Zou, X. Zhuge, and F. Weng, "Characterization of bias of Advanced Himawari Imager infrared observations from NWP background simulations using CRTM and RTTOV," *J. Atmos. Ocean. Technol.*, vol. 33, pp. 2553–2567, 2016.

[11] X. Zhuge and X. Zou, "Test of a modified infrared-only ABI cloud mask algorithm for AHI radiance observations," *J. Appl. Meteor. Climatol.*, vol. 55, pp. 2529–2546, 2016.

[12] T. Zhu, D.-L. Zhang, and F. Weng, "Impact of the advanced microwave sounding unit measurements on hurricane prediction," *Monthly Weather Rev.*, vol. 130, pp. 2416–2432, 2002.

[13] J. L. Demuth, M. DeMaria, J. A. Knaff, and T. H. Vonder Haar, "Evaluation of advanced microwave sounding unit tropical-cyclone intensity and size estimation algorithms," *J. Appl. Meteor. Climatol.*, vol. 43, pp. 282–296, 2004.

[14] J. A. Knaff, S. A. Seseske, M. DeMaria, and J. L. Demuth, "On the influences of vertical wind shear on symmetric tropical cyclone structure derived from AMSU," *Monthly Weather Rev.*, vol. 132, pp. 2503–2510, 2004.

[15] J. L. Demuth, M. DeMaria, and J. A. Knaff, "Improvement of advanced microwave sounding unit tropical cyclone intensity and size estimation algorithms," *J. Appl. Meteor. Climatol.*, vol. 45, pp. 1573–1581, 2006.

[16] R. Gutro, *NASA Satellite Gets an Eye-Opening Look at Super Typhoon Jelawat*. May 25, 2018. [Online]. Available: https://www.nasa.gov/feature/goddard/2018/jelawat-western-pacific-ocean
[17] M. Tian, X. Zou, and F. Weng, "Use of Allan deviation for characterizing satellite microwave sounder noise equivalent differential temperature (NEDT)," *IEEE Geosci. Remote Sens. Lett.*, vol. 12, no. 12, pp. 2477–2480, Dec. 2015.
[18] M. D. Goldberg, D. S. Crosby, and L. Zhou, "The limb adjustment of AMSU-A observations: Methodology and validation," *J. Appl. Meteorol. Climatol.*, vol. 40, pp. 70–83, 2001.
[19] K. Zhang *et al.*, "A methodology to adjust ATMS observations for limb effect and its applications," *J. Geophys. Res.*, vol. 122, pp. 11347–11356, 2017.
[20] X. Tian, X. Zou, and S. Yang, "A limb correction method for MWTS-2 and its applications," *Adv. Atmos. Sci.*, vol. 35, pp. 1547–1552, 2018.
[21] N. Atkinson, "Annex to AAPP scientific documentation: Pre-processing of ATMS and CrIS," Document NWPSAF-MO-UD-027, version 1.0, 2011.
[22] S. S. Chen, J. A. Knaff, and F. D. Marks, Jr., "Effects of vertical wind shear and storm motion on tropical cyclone rainfall asymmetries deduced from TRMM," *Monthly Weather Rev.*, vol. 134, pp. 3190–3208, 2006.
[23] R. L. Elsberry and R. A. Jeffries, "Vertical wind shear influences on tropical cyclone formation and intensification during TCM-92 and TCM-93," *Monthly Weather Rev.*, vol. 124, pp. 1374–1387, 1996.
[24] R. Rogers, S. Chen, J. Tenerelli, and H. Willoughby, "A numerical study of the impact of vertical shear on the distribution of rainfall in Hurricane Bonnie (1998)," *Monthly Weather Rev.*, vol. 131, pp. 1577–1599, 2003.
[25] Y. Ma, X. Zou, and F. Weng, "Potential applications of small satellite microwave observations for monitoring and predicting global fast-evolving weathers," *IEEE J. Sel. Topics Appl. Earth Observ. Remote Sens.*, 2017.

Xiaolei Zou (A'11–M'18) received the Ph.D. degree from the Institute of Atmospheric Physics, Academia Sinica, Beijing, China, in 1988.

She was with the National Center for Environmental Prediction, College Park, MD, USA, where she was involved in medium-range global forecast model four-dimensional variational data assimilation (4-D Var) system with full physics from 1989 to 1993, and the fifth-generation Penn State/National Center for Atmospheric Research Mesoscale Model (MM5) 4-D Var system from 1993 to 1997. Since 1993, she has been involved in global positioning system radio occultation data assimilation. From 1997 to 2014, she was a Professor with the Department of Earth, Ocean, and Atmospheric Science, Florida State University, Tallahassee, FL, USA. Since 2014, she has been with the Earth System Science Interdisciplinary Center, University of Maryland, College Park, MD, USA, where she is involved in satellite data assimilation for quantitative precipitation forecasts and hurricane track and intensity forecasts. She has authored more than 150 papers in peer-reviewed journals.

Dr. Zou was a recipient of the 2008 American Meteorological Society Fellow Award for her outstanding contributions to the applications of satellite data in the numerical-weather-prediction models and the education in data assimilation.

Xiaoxu Tian received the B.S. and M.S. degrees in earth, ocean, and atmospheric science from Florida State University, Tallahassee, FL, USA, in 2012 and 2014, respectively, and the Ph.D. degree in atmospheric and oceanic science from the University of Maryland, College Park, MD, USA, in 2017.

He is currently a Postdoctoral Associate with the Earth System Science Interdisciplinary Center, University of Maryland. His research interests include retrievals of three-dimensional thermal structures in tropical cyclone cases with radiance measurements from satellite microwave instruments and development of four-dimensional variational data assimilation systems for hurricane vortex initializations.